Transverse compaction of twisted carbon yarns: Experiment and elasto-plastic Mohr–Coulomb modeling

Marcello Rubino, Yanneck Wielhorski, Stéphane Roux

Transverse compaction of twisted carbon yarns: Experiment and elasto-plastic Mohr-Coulomb modeling

Marcello Rubino[a,b], Yanneck Wielhorski[b,*], Stéphane Roux[a]

[a] *Université Paris-Saclay/CentraleSupélec/ENS Paris-Saclay/CNRS, LMPS, 4, Avenue des Sciences, 91192 Gif-sur-Yvette, France*
[b] *Safran Aircraft Engines, Rond-point René Ravaud, 77550 Moissy-Cramayel, France*

Abstract

The mechanical characterization of the carbon yarns, the major component of woven textiles for composite materials, is essential for optimizing the fabrication and the final properties of such materials.

This work focuses on carbon yarns formed by twisting several elementary tows, each composed of thousands of carbon fibers, whose weak cohesion is ensured by a sizing agent. Different twist magnitudes are studied in dry and wet conditions. Transverse compaction tests are performed with loading-unloading cycles of increasing amplitudes. They have shown that the yarn cross section approaches a critical state where the fiber volume fraction remains constant, irrespective of twist level and humidity.

The experimental results evidence an elasto-plastic behavior, analogous to that of a 2D granular medium. A simple model is proposed with a cohesive non-associated Mohr-Coulomb plasticity, having very few constitutive parameters. The effect of twist, water, and sizing can be accounted for.

Keywords: Carbon yarn, Twisting yarn, Granular media, Mohr-Coulomb plasticity

1. Introduction

Woven composites are becoming key elements in many manufactured parts, particularly for the aeronautics [1] and automotive [2] industries. These composites contribute to lighter structures, thus reducing fuel consumption while maintaining excellent mechanical properties.

These excellent specific features are mainly due to the complex microstructure of these entangled fibrous materials, often composed of carbon, glass, or ceramic yarns. The stiffness and strength along the yarn axis are outstanding. However, in the transverse direction, the matrix controls the mechanical behavior, which is generally much weaker. To mitigate the effect of this large contrast,

*Corresponding author.
Email address: yanneck.wielhorski@safrangroup.com (Yanneck Wielhorski)

weaving offers a wide range of different architectures (up to 3D weaving) to engineer and optimize multiaxial mechanical performances [3, 4, 5, 6]. More generally, the entire manufacturing process plays a crucial role in optimizing the mechanical behavior of the composite since each step can modify the structure of the reinforcement [7].

To study the deformations occurring during the draping of dry textile reinforcements, many works [8, 9] are devoted to characterizing the mechanical behavior of fibrous preforms through experiments and macroscale simulations for hemispherical forming as well as bending and biaxial tensile tests [10, 11, 12, 13, 14, 15].

However, a mesoscopic mechanical analysis of woven reinforcements allows the mechanical phenomena occurring at this scale to be more faithfully captured. As such, a recent study [16] provides a very good fit for a variety of different tests on 3D woven fabrics (through-thickness compression, uniaxial and biaxial tension, and in-plane shear).

This stresses the importance of a good characterization of the yarns themselves, not only in the longitudinal direction but also transversally. Indeed, a yarn by itself displays a subtle arrangement of the different fibers of its constituting tows inherited from the twisting, and its internal cohesion is quite essential. While the microscale remains out of reach (the number of elementary fibers is prohibitively large), a vast literature was devoted to representing yarn mechanical behavior at two main scales [8, 17, 18]: mesoscale and sub-mesoscale (also often called microscale).

Mesoscale approaches aim to characterize transverse properties using hyper- [16, 19, 20] or hypo-elastic [21] laws, assuming a homogeneous representation of the yarn. While these models are powerful, they require the identification of numerous constitutive parameters, which is very challenging experimentally.

Sub-mesoscale models attempt to describe the behavior of the constitutive model from an elementary description of the constituting fibers, assuming that contact and friction are the main phenomena responsible for the (mesoscale) yarn behavior [16, 22, 23, 24, 25, 26]. However, the number of filaments in classical yarns (often several tens of thousands) is inaccessible. When the number of fibers tends to infinity, a non-trivial asymptotic (homogenized) behavior exists and no longer depends on the number of fibers; it is thus appealing to introduce "virtual" fibers, each grouping multiple actual fibers. One difficulty is thus to characterize the properties of the virtual fibers, often assumed to be elastic. This approach captures irreversible deformations observed during the manufacturing process with few constitutive parameters. Still, it comes with a significant computational cost due to solving the

numerous contact and friction events between the fibers, whose "non-smooth" behavior is well-known to call for a computationally demanding treatment. Additionally, the initial disposition of the fibers in sub-mesoscale models can lead to unrealistic choices (particularly for the yarn twist) that strongly impact the observed macroscopic behavior. An alternative attractive choice would be to resort to the homogenized mechanical behavior, but this route has not been explored to the best of our knowledge.

To guide the choice of appropriate modeling, this article presents an experimental investigation focused on the transverse compaction of carbon yarns. The yarn thickness, width, and fiber volume fraction (FVF) during the compaction process are analyzed for different yarn types, humidity (wet or dry), and twist levels.

Building upon the experimental observations, it is proposed to account for the transverse mechanical behavior of the yarns as a continuous homogeneous solid (in the spirit of a mesoscale approach) whose constitutive law results from the homogenization of the fibrous microstructure. Thanks to the broad field of imaging techniques, the yarn cross section geometry can be estimated all along the compression cycles. The experimental observations suggest an elasto-plastic material response for carbon and glass yarn.

The outline of the present paper is the following: Section 2 gives an overview of the different tested yarns, the experimental setup, and its exploitation. Section 3 presents the obtained results on the transversal compression tests performed on carbon yarns at different twisting levels. Section 4 recalls the theoretical fundamentals of the proposed Mohr-Coulomb-based elasto-plastic law and shows that it requires very few parameters. This law is implemented in a Finite-Element software, allowing for simulating of the transverse compaction test, whose results are presented in section 5. Finally, section 6 provides a conclusion emphasizing the significance of the proposed elasto-plastic description and suggests future research directions.

2. Materials and Methods

2.1. Carbon yarns

This study focused on 48,000 fiber yarns twisted from four tows, each consisting of 12,000 fibers. The elementary 12k tows are produced by two different suppliers, and their properties are summarized in Table 1. The first type, called IM7, is the carbon fiber produced by Hexcel. Referring to the manufacturer's data, the fiber diameter is 5.2 $\pm$ 0.2 µm, and the Young's modulus is 276 GPa. A DGEBA resin epoxy and pluronic F68 surfactant is used as a sizing agent. The second one, named

Fiber type	**IM7** (Hexcel)								**T1100** (Toray)							
Fiber diameter ⌀ (µm)	5.2 ± 0.2								5.5 ± 0.2							
12k tow density (tex)	446								493							
Humidity	dry				wet				dry				wet			
tpm	10	20	30	50	10	20	30	50	10	20	30	50	10	20	30	50

Table 1: Different yarn types tested by the transversal compression device.

T1100, is produced by Toray. The manufacturer's data indicate a fiber diameter of 5.5 ± 0.2 µm and Young's modulus of 324 GPa. The sizing agent contains a DGEBA resin epoxy.

Moreover, in order to study the influence of twist, four different levels have been chosen: 10, 20, 30, and 50 turns per meter (tpm).

It is important to recall that during the weaving, the loom is sprayed with demineralized water in order to wet the yarns and for draping, the fibrous reinforcement is also heavily wetted. It is expected that this humidity has a drastic impact on friction, and hence on the yarn mechanical behavior, motivating its experimental investigation, although the question is very seldom addressed in the literature. Therefore, the yarns were analyzed under wet conditions by completely immersing them in a container of demineralized water for about 15 minutes for complete saturation. Then, the yarn was allowed to be drained for a period of 30 minutes on an absorbent cloth so that only the entrapped water held by capillarity would remain.

2.2. Experimental setup

A compaction testing machine (see figure 1) was designed specifically for performing a yarn diametral compression. The yarns are compressed between a circular metal plate of 50 mm diameter and a fixed transparent sapphire plate, below which a blue laser profilometer, Keyence VJ-6700 was placed. It offered a 20 µm lateral resolution. Along the yarn axis, the laser beam size was set to 100 µm. A set of weights and pulleys provide a low longitudinal yarn tension for the proper positioning of the yarn in the machine, allowing both to keep the yarn horizontal and to select the segment to be compressed. A lateral screw system allows the locking of the yarn after positioning and before compression. A dynamometer measures the axial force applied to the yarn by the screw system. Finally, an axial motor drives the profilometer longitudinally after each lateral yarn profile acquisition. Thus a complete 2D (longitudinal and transverse) map is scanned and recorded. To avoid the possible influence of boundary conditions on the experimental results, only a central portion of 40 mm of the compressed yarn is analyzed with the profilometer.

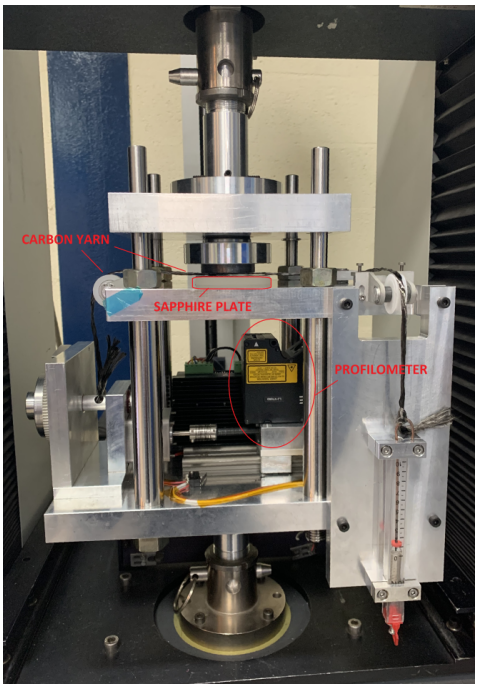

Figure 1: Transverse compaction: test testing machine.

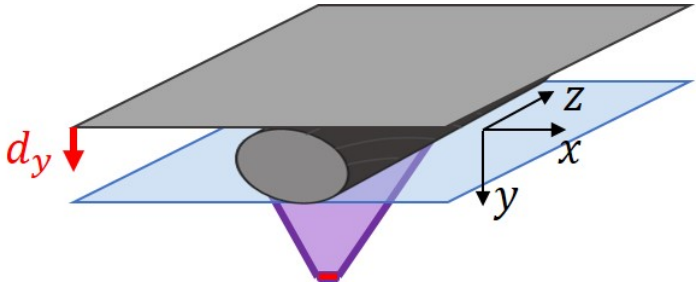

Figure 2: Schematic representation of the transversal compaction. The purple triangle shows schematically one profile scanned by the profilometer.

The transverse compaction test, at a 0.1 mm.min^{-1} velocity, consists of five repeated loading-unloading cycles in which the load increases at each cycle while the unloading is stopped at the same level of reaction force, 50 N, measured by a load cell. This value was set not to introduce a major perturbation in the fiber organization.

2.3. Image post-processing

Let the z axis be aligned with the yarn length, y the compression direction (vertical in our set-up), and x the cross section direction in the observation window (see figure 2).

The measurement is a profilometry map of the compressed yarn. The image gray level encodes the

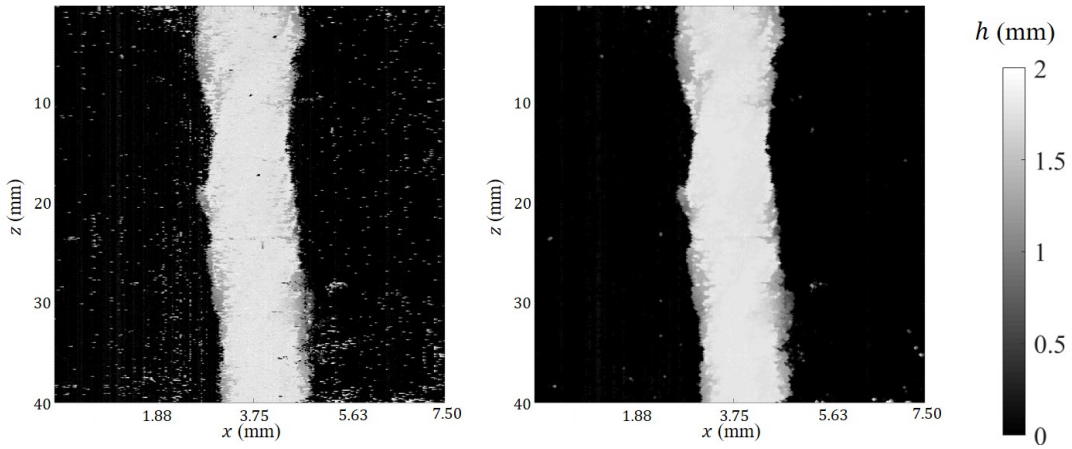

(a) (b)

Figure 3: Resulting profile image: (a) raw image, (b) pre-filtered image using closing/opening operations.

y-position of the fibers (integrated over the laser spot size (20×100 µm^2) with respect to the metal plate). Figure 3a shows one profile of the initial state of a carbon yarn twisted at 30 tpm. As can be seen in this figure, the measured maps are noisy, especially in the background. A large part of the noise can be suppressed by successive opening and closing morphological filters as illustrated in figure 3b. Moreover, the yarn surface appears to be very flat, in close contact with the sapphire window. The yarn thickness h can be easily estimated as the maximum gap between the yarn and the metal plate surface (this information is more precise than the direct measured displacement of the compression plate).

Even if the initial goal was to map the details of the yarn section topography when not contacting the lower compression plate, the useful part of the images rather lies in the yarn boundary as if they were binary. Thus, they must be processed to estimate the position of the left and right boundaries, denoted as $x_l(z)$ and $x_r(z)$ respectively.

Each boundary is processed independently, hence only the left one will be described here. The image is first cut at a maximum x value that lies in the yarn for all z. Its gray levels are further normalized between 0 (background) and 1 (yarn), and the resulting image is called $J_l(x,z)$. Then a cost function is defined as the L_2 norm of the residual between the cropped normalized image and its binary representation

$$\mathcal{T}[x_l(z)] = \frac{1}{2}\sum_{z\in\Omega_z}\left(J_l(x,z) - \mathcal{H}(x - x_l(z))\right)^2 \tag{1}$$

where $\mathcal{H}$ designates the Heaviside function.

The problem is further regularized with a coarse discretization of $x_l(z)$ using a one-dimensional regular mesh and piecewise linear shape functions

$$x_l(z) \approx \sum_i \xi_i \cdot \psi_i(z) \tag{2}$$

whose amplitudes are collected in a vector $\{\boldsymbol{\xi}\}$. A further regularization can be introduced in the form of a penalty given to the square of the (discrete) boundary curvature

$$\mathcal{T}_{\text{reg}}[x_l(z)] = \frac{F}{2} \sum_{i=2}^{N-1} (2\xi_i - \xi_{i-1} - \xi_{i+1})^2 \tag{3}$$

where the weight F can be tuned at will. It is chosen as having a large value initially and relaxed to a small value once the boundary position begins to settle onto a stationary solution. This nonlinear minimization problem is solved using an iterative Newton-Raphson scheme.

Finally, having estimated both left and right boundaries, using the same procedure, the yarn width w is calculated as

$$w(z) = x_r(z) - x_l(z) \tag{4}$$

Because the yarn cross section is considered as being a mere rectangle for each z, the FVF is computed from its mean area $A_t = h\langle w(z)\rangle_z$ (where $\langle ...\rangle_z$ denotes an average over z). Since the total area of carbon fibers cross section, $A_s = N(\pi/4)\varnothing^2$, remains constant, the 2D-defined packing factor ϕ_{2D} is defined as

$$\phi_{2D} = \frac{A_s}{A_t} \tag{5}$$

Let us stress that this estimate is approximative, in particular because of the a priori rectangular picturing of the cross section. Experimentally, even for moderate loads, the yarn is in very close contact with the observation window and presumably with the opposite compression plate. So both upper and lower yarn surface are flat. Thus, the main point to elucidate is the shape of the free surfaces on the sides of the yarn. Unfortunately, despite an accurate optical sensor, it was difficult to do more than the identification of the yarn "projection". Hence, in a first approximation, the geometry of the cross section is chosen rectangular. Other geometries could easily be considered, such as the race-track, but the section aspect ratio under compression is such that the difference between a race-track

and a rectangle is negligible. In the low load range, and for high twist levels, such a simplification may not be accurate. This is yet another argument for not reaching a complete unload in between cycles. It is noteworthy that whereas this rectangular approximation is indeed selected for calculating the experimental yarn packing factor ϕ_{2D}, the race-track geometry has been chosen as cross section initialization for the further FE simulations to avoid angular points (cf. section 5).

3. Experimental results

3.1. Mechanical response

Figure 4 illustrates the force-displacement data of loading-unloading cycles for a 30 tpm IM7 yarn in both dry and wet conditions.

These interesting curves demonstrate an elasto-plastic behavior in this both conditions. A strong stiffening akin to an exponential law is observable while it is possible to capture an apparently linear elastic behavior when unloading the compressed yarn. It is noteworthy that the plastic strains are less pronounced while the compression becomes stronger. This is due to different effects. First, the yarn contact surface with the plates increases while the thickness decreases. Second, the yarn fiber fraction reaches its critical value, where the tangent modulus is higher than in its initial loose state. Thus, further compaction implies shear band reflection on the plates in contact and slips along these interfaces. This implies an exponential build-up of pressure from the edge to the yarn axis and an increased friction. All these effects contribute to rendering further plastic strains more and more difficult.

Moreover, the experimental results emphasize that, at a given value of the vertical force, the yarn thickness is lower in the wet case than in the dry one. This is attributed to a lower mobilized friction when the yarn is wet.

3.2. Thickness evolution

From the post-processed images, one can estimate the mean compression stress σ_{yy} from the compression force and yarn area in contact with the plate (mean measured width multiplied by the known compressed yarn length). Hence, at this stage, besides the mean compressive stress, it is difficult to argue for finer information. Thus, the observed data is plotted as mean stress vs mean strain.

However, this assumption has no further consequences. Indeed, from the qualitative observations, a suited constitutive law will be formulated, and its parameters identified through an optimal matching

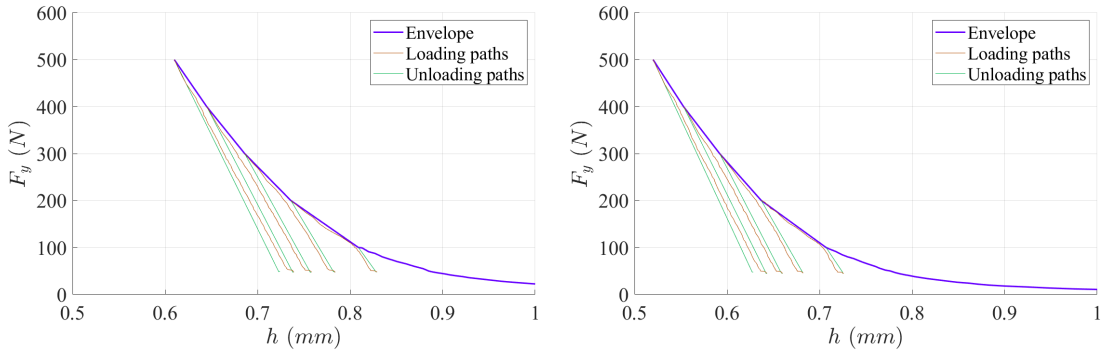

Figure 4: Mechanical response of loading-unloading cycles on a IM7 yarn (30 tpm): (a) dry and (b) wet conditions.

of global observations (force, thickness) with simulated quantities. Thus, the following identification will take into account the uneven stress distribution underneath the contact surface.

Similarly, the Hencky strain ε_{yy} is computed along the compression axis. The corresponding stress-strain curves are shown in figure 5. Let us note that the initial state of the yarn is ill-defined. As seen in figure 4, very large and irreversible changes in the initial thickness h_0 can result from a vanishing transverse force. The consequence is that stress strain curves appear to display huge differences in between different tests. Changing h_0 implies a mere translation of the Hencky strain. It is proposed to define h_0 conventionally so that the stress-strain curves coincide for large stress. Figure 6 shows that this procedure leads to an excellent collapse of all curves onto a master one, independently of the twist. The vertical stress presents different maximum values given that the contact area of the yarn with the metal plate is larger for the less twisted yarns.

3.3. Width evolution

Regarding the evolution of width, a horizontal Hencky strain ε_{xx} is computed (refer to figure 7). Given the difficulty in correctly estimating the initial state, and hence the strains in absolute fashion, a similar procedure as above can be followed, namely adjusting the initial width, w_0, from the exploitation of the large stress data where the sensitivity to the preparation stage has been erased. Figure 7 shows the resulting strain evolution. Let us emphasize that the ε_{xx}–ε_{yy} curves, all exhibit a final slope of 1 (this would be true irrespective of the definition of h_0 and w_0, but the redefinition of the initial state allows for the same asymptote to hold irrespective of the twist).This indicates that the yarn cross section reaches a state of constant area. Because of the decoupling between the cross section and the yarn axis ($\varepsilon_{zz} = 0$), this means that the packing factor has reached a constant value, (*i.e.*,

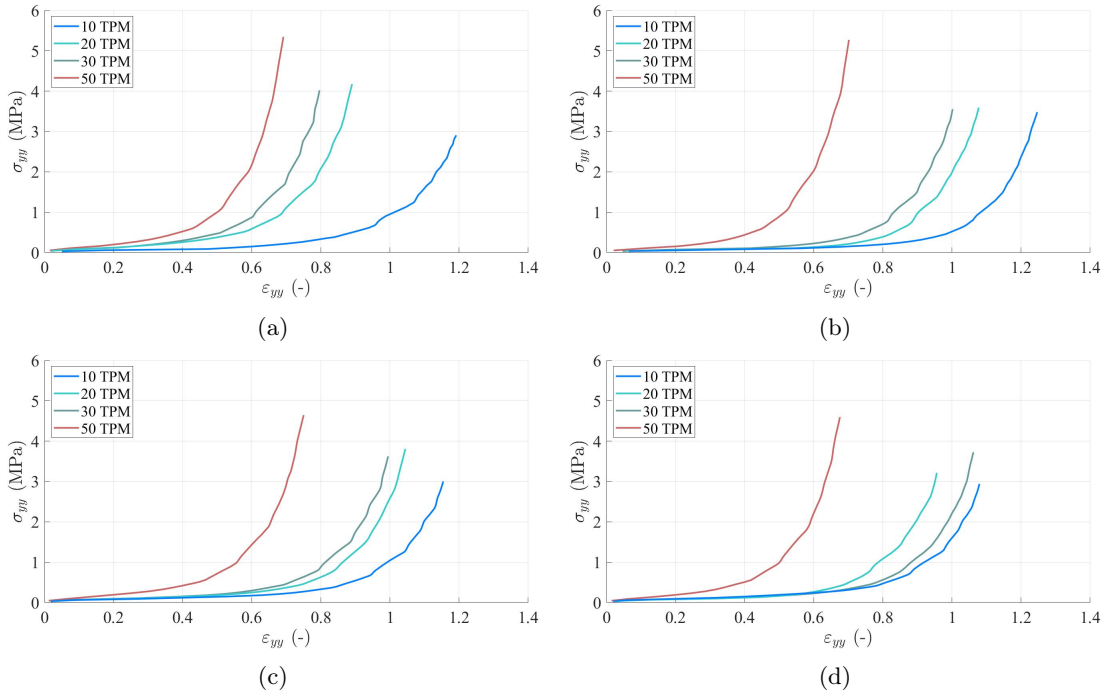

Figure 5: Evolution of the vertical Hencky strain ε_{yy} during transversal compaction test: top row ((a) dry and (b) wet) IM7 fiber yarn; bottom row ((c) dry and (d) wet) T1100 fiber yarn.

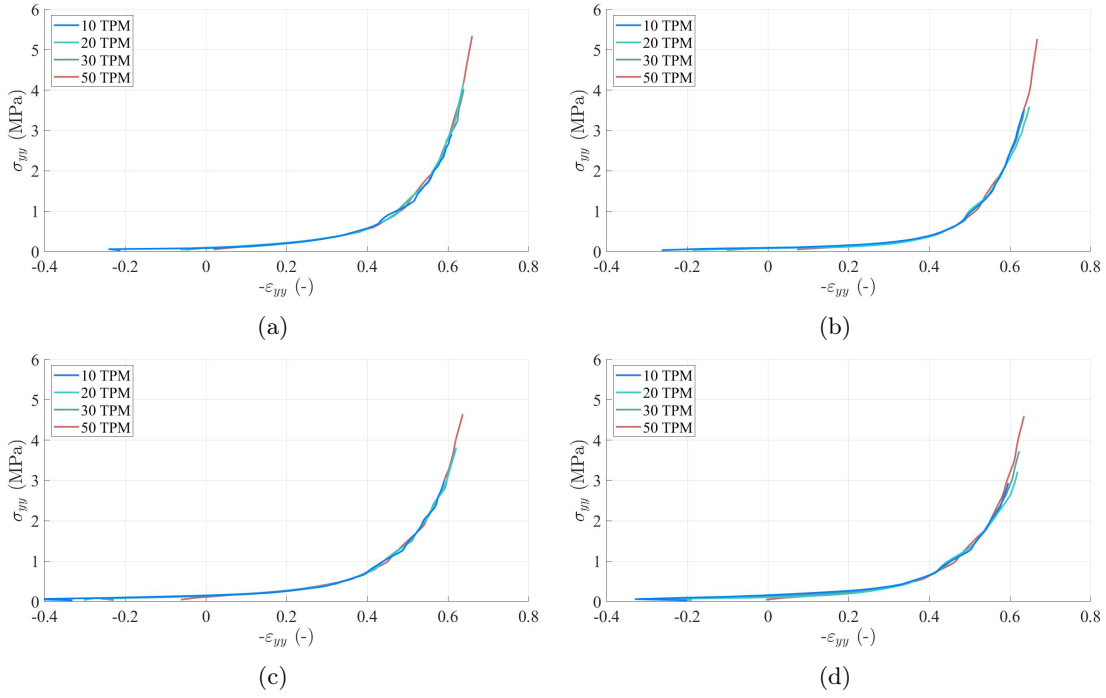

Figure 6: Evolution of the vertical Hencky strain ε_{yy} during transversal compaction test after horizontal translation: top row ((a) dry and (b) wet) IM7 fiber yarn; bottom row ((c) dry and (d) wet) T1100 fiber yarn. All curves almost perfectly match.

constant FVF). This is a very important point that will be further referred to as the *"critical state"* and discussed in the modeling.

3.4. FVF evolution

Finally, the evolution of the FVF for the four twist levels is shown in figure 8. In both yarn types and dry and wet conditions, after initial rapid growth, the value of the FVF stabilizes for most of the tests. This curve portion corresponds to the critical state where a constant cross section area — *i.e.*, incompressibility for a 2D solid — was already reported.

Finally, concerning the humidity conditions, what distinguishes wet from dry yarns is how quickly the asymptotic isochoric regime is reached. In wet yarns, the transition from compressible to incompressible is very abrupt (with the exception of 50 tpm), while it is more gradual in dry conditions.

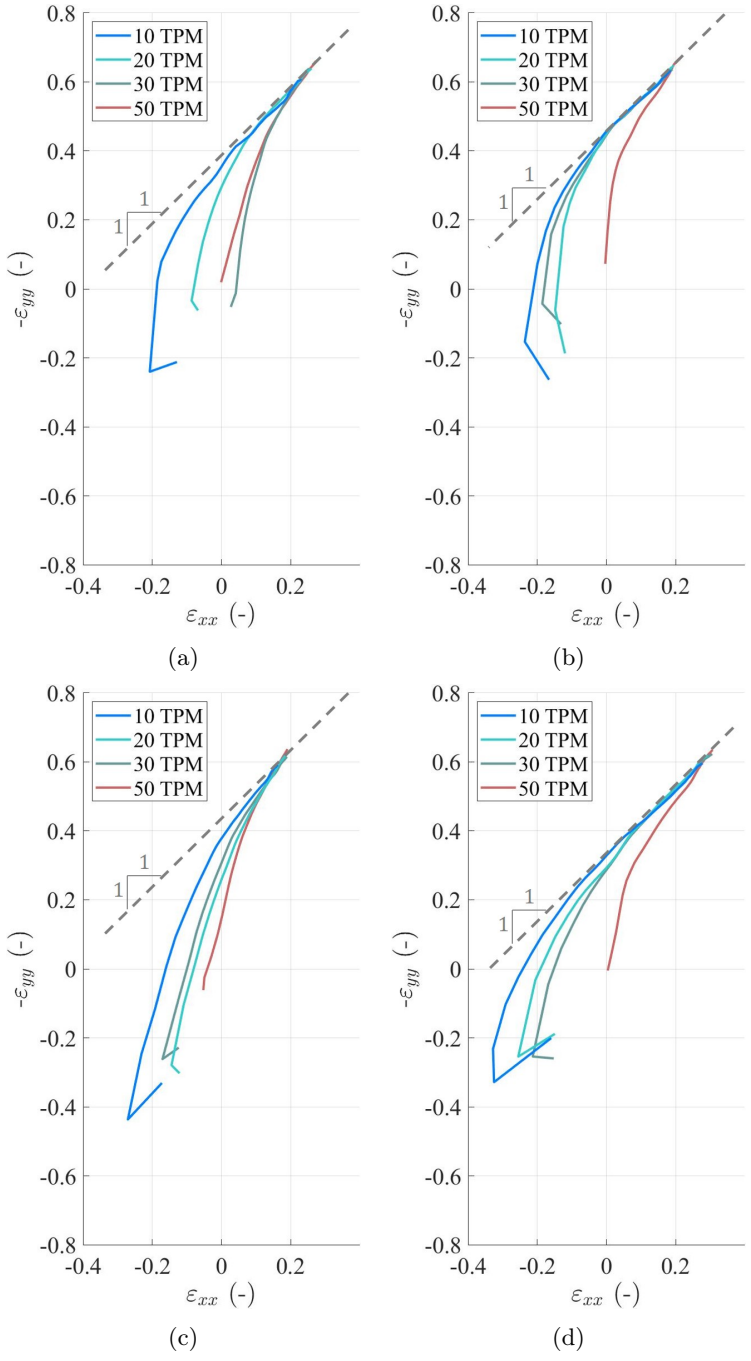

Figure 7: Horizontal Hencky strain ε_{xx} as function of the vertical Hencky strain ε_{yy}: top row ((a) dry and (b) wet) IM7 fiber yarn; bottom row ((c) dry and (d) wet) T1100 fiber yarn. One can see that the final slope of all curves is 1, indicating an isochoric transformation.

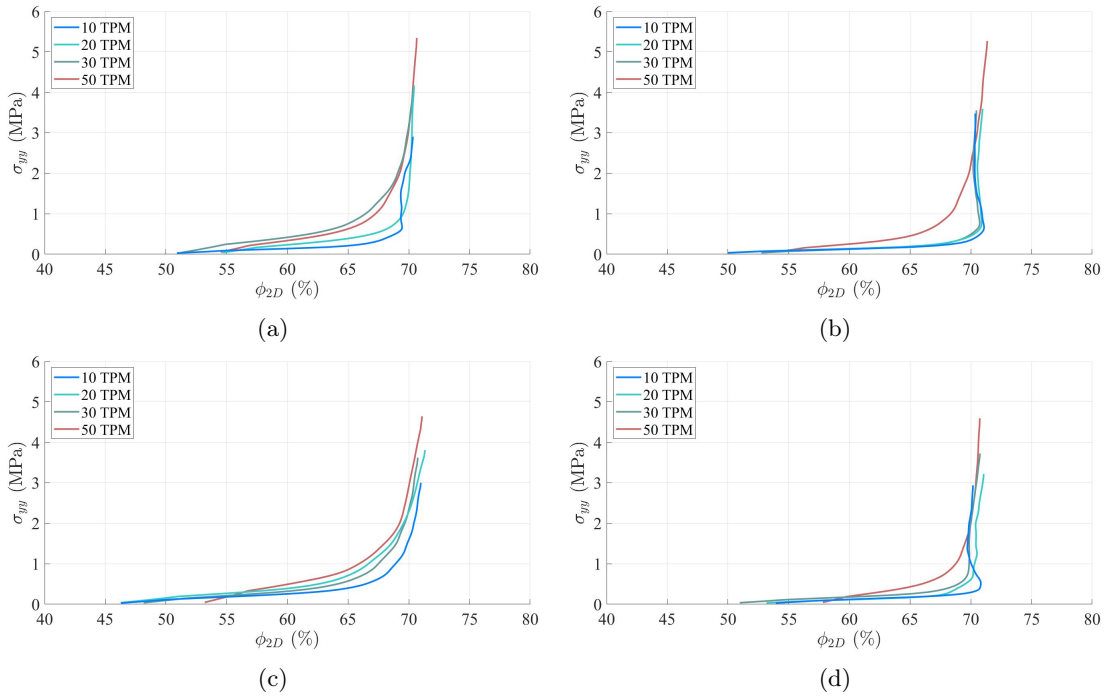

Figure 8: Evolution of FVF during transversal compaction test: top row ((a) dry and (b) wet) IM7 fiber yarn; bottom row ((c) dry and (d) wet) T1100 fiber yarn.

4. Elasto-plastic law

4.1. Towards an elasto-plastic law

Yarns are challenging to model for obvious reasons: they are highly flexible, and hence finite strain theory is needed, and they can exhibit huge contrast in their stiffness (*e.g.*, very stiff under longitudinal tension but very compliant under compression as buckling is very easy). These observations prompted many attempts to propose a general framework for the constitutive law of yarns first as a hypo-elastic medium [10, 21, 27]. This allows one to deal with large strains but shows difficulties with non-conservative loading paths. Hyper-elasticity can be seen as a particular case of hypo-elasticity and offers a more secure framework for having a consistent thermodynamic description. However, the intrinsic anisotropy of yarns (at least transversally isotropic if the twist is ignored) leads to the formulation of elastic energy based on five strain invariants, where only two are involved in the case of transverse compaction, namely the spherical and deviatoric part of the 2D (x, y) strain (and similarly for stress).Moreover, very significant non-linearities are observed, thus leading to the use of large-order polynomial expansion based on these invariants to adjust the hyperelastic potential energy. This implies a large number of constitutive parameters and the need to perform many sophisticated experiments

for their identification. Alternatively, one may postulate some truncation of the potential energy (*e.g.*, ignoring the coupling between different invariants). Still, the resulting simplification is fragile (*i.e.*, not based on a solid theoretical justification) and not entirely consistent with the starting point of using a very general theory. Moreover, the mechanical behavior of carbon yarns under transversal compression discussed in the previous section shows significant irreversible deformations, typical of an elasto-plastic behavior, which hyper- or hypo-elastic models cannot describe.

One may fear that adding plasticity to this problem may further increase the number of model parameters, but, as it will be shown, this leads to a significant simplification. It can also be argued that even an elasto-plastic behavior can be modeled as hyper-elastic, provided the loading path is simple (radial and monotonous). However, in practice, unloading is very common in textile processing, and hence, the previously reported behavior cannot be described by a hyperelastic law.

When observing the yarn cross section, the analogy with an ideal 2D granular medium composed of uniform disks (or cylinders) is striking (as only yarn twist has no counterpart in this parallel, but since the fiber angle induced by the twist is very small (even for the highest twist considered here), it is natural to address twist as a small perturbation to the 2D granular medium leading order description). Indeed, such systems were introduced long ago by Schneebeli [28] and further investigated both experimentally and numerically to understand the micro-mechanics within soils better. Essentially, in such Schneebeli's models, the elastic deformation of the cylinders can be neglected (they can be considered rigid). Yet, the assembly can undergo large deformations by the opening or closing of contacts and solid friction. This is an emblematic example of non-smooth mechanics [29] when describing the "grains" themselves [30].

Let us quickly recall what has been understood from such works. First, as often postulated in hyper-elastic models, in these 2D models, there is no coupling with the longitudinal direction, and the z direction plays no role in the reported experiment (no axial strain). In Schneebeli's models, in the (x, y) plane, a two-dimensional rigid-plastic behavior prevails because the cylinders can be considered rigid (non-deformable) and friction is supposed to be ruled by Coulomb's law. Starting from an equilibrium state, if all interfiber (*i.e.*, intergrain) forces are multiplied by an arbitrary (positive) factor, the same state remains in equilibrium (such a situation cannot be replicated with hyper-elastic theory). This has far-reaching consequences: only the "direction" of the (2D) stress tensor matters and not its magnitude. Assuming isotropy in this cross section, two stress invariants may come into play, namely hydrostatic (*i.e.*, pressure) and deviatoric. When the ratio of deviatoric over spherical

part is smaller than the tangent of the *friction angle*, no motion is possible (a case of infinite stiffness again inaccessible for hyperelastic theory). When reaching the friction angle, flow takes place whose magnitude is ruled by plasticity theory (namely, stress should remain on the plastic limit). Therefore, only one parameter is needed to describe the plastic limit. Similarly, only the direction of the strain rate matters. Macroscopically, the ratio between the spherical part of the strain rate and its deviatoric part is relevant. This defines the *dilatancy* angle. Since Coulomb's friction is at play between cylinders, plasticity cannot be "associated", and hence, the dilatancy and friction angles differ.

Such media behavior depends on their "preparation". They can be in a "loose" or "dense" state, parametrized by a single scalar parameter, the compacity or surface (volume) fraction. Under shear, this initial state is progressively forgotten, and the volume fraction tends to a unique value, corresponding to the "critical state". Since the volume fraction does not change at this stationary state, the dilatancy angle is null. Hence, the friction angle is the only constitutive parameter needed to describe such a medium under large shear, and its compacity is uniquely defined.

Before reaching this critical state, again assuming isotropy, the difference δ in volume fraction with its value in the critical state can be used as the only relevant internal variable. Based on the same argument as previously, only the dependence of the friction angle, φ, and of the dilatancy angle, ψ with δ is sufficient to describe the constitutive law. Moreover, because δ can be treated as a small perturbation, ψ is to dominant order a linear function of δ. This relation controls the dilatant/contractant feature of the medium under shear, hence the evolution of δ (or the hardening law) for dense/loose states, respectively. Similarly to the dilatancy angle, the friction angle is to dominant order an affine function of δ. Thus, even enriching the behavior to include a varying volume fraction leads to no more than three constitutive parameters, $\varphi(\delta = 0)$, $\partial\varphi/\partial\delta$ and $\partial\psi/\partial\delta$. Finally, Taylor's assumption states that the two latter quantities are equal

$$\frac{\partial\varphi}{\partial\delta} = \frac{\partial\psi}{\partial\delta} \tag{6}$$

reducing the number of unknowns to *only two*. Notably, despite the plastic behavior's complexity, the number of effective parameters is extremely small. This is known as 2D Mohr-Coulomb plasticity. Let us note that in 3D, there are two variants, Mohr-Coulomb and Drucker-Prager, but in 2D, they are identical.

Looking back to the experimental results described in section 3, it is now quite clear that the observed isochoric regime is actually identical to the critical state. Therefore, the corresponding FVF

should be *an intrinsic property common to all yarns*, (again a result that cannot be derived from a macroscopic phenomenological description) independently of their twist, of the presence of water or of tow suppliers (unless some fiber diameter polydispersity would distinguish them). The same remark for $\partial\psi/\partial\delta$ can be made. Because of the sizing formulation, only the friction angle in the critical state should depend on the wet/dry state and on the tow manufacturer.

Yet, the Schneebeli's model does not capture all the observed features of the yarns:

- The yarn initially has some *cohesion* due to the sizing agent and the presence of water in the wet state through capillary forces. This effect can be introduced in the continuum by offsetting the plastic limit.
- The twist is not accounted for in the 2D granular system (nor is it in the hyperelastic models). As emphasized previously, the twist is expected to be a small perturbation because of the low angle between fibers and yarn axis. Yet, it may introduce a small coupling between cross section deformation and axial stress. Indeed, if no axial displacement is considered, the transverse compression induces a longer fiber path length for some of them, which can only be mitigated by tow side-motion or cross section additional stress (akin to a surface tension) and fiber slip, assuming their inextensibility.
- When unloaded, the yarn shows a linear elastic behavior. Presumably, this elasticity is not due to the fiber response but rather to the sizing that coats the fibers. It may also receive a contribution from the yarn twisting, as mentioned above. Because of decoupling with the axial direction and the isotropy assumption in the cross section plane, Young's modulus and Poisson's ratio are needed.

The following section discusses the elasto-plastic behavior, considering the fiber bundle as a 2D granular medium through the Mohr-Coulomb yield criterion. Then, the identification procedure for analyzing the elasto-plastic behavior is described, and the identified parameters are discussed. Let us stress that implementing such behavior in modeling represents an original approach, as most FE solvers assume an identical behavior in all directions.

4.2. Mohr-Coulomb yield criterion

One of the most widely used plastic laws in soil mechanics is the Mohr-Coulomb yield criterion [31], as expressed in equation (7). This criterion defines a limit surface for plasticity mobilization in Mohr's plane (τ_n, σ_n), where τ_n represents the shear component and σ_n denotes the normal component of the stress vector on a plane of normal n (in the proposed convention, positive values denote traction), as illustrated in the schematic diagram of figure 9. This criterion takes into account the friction angle φ, which is an important parameter in the plasticity of granular media. The tangent of this angle denotes

the limiting slope with respect to the horizontal plane at which a piled granular media may start to slump. Note that for a cohesionless material, the criterion is a straight line whose slope defines the friction angle. Cohesion can be included by a mere offset of this "cone"

$$|\tau_n| = c - \sigma_n \tan\varphi \tag{7}$$

The same criterion can be described in terms of the deviator stress, s, and mean stress, p

$$s = \sqrt{\left(\frac{\sigma_{xx} - \sigma_{yy}}{2}\right)^2 + \sigma_{xy}^2} \tag{8}$$

$$p = \frac{\sigma_{xx} + \sigma_{yy}}{2} \tag{9}$$

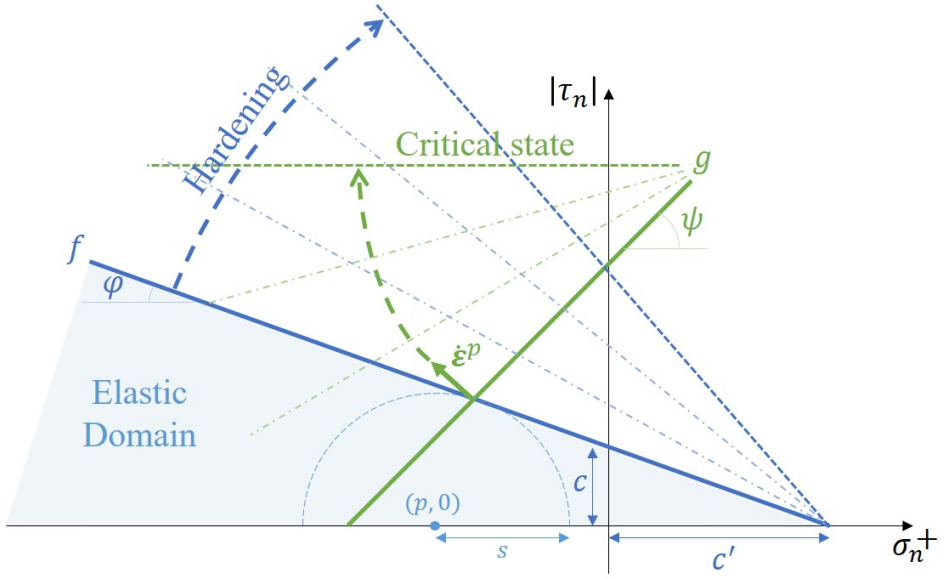

Figure 9: Scheme of the Mohr-Coulomb yield criterion, in blue, and the proposed hardening rule until the critical state. The plastic potential, in green, has an opposite slope (negative dilatancy angle), so the plastic strain rate points towards the left (contraction) during the compaction test but varies its direction until a complete isochoric transformation.

Here, s represents the radius of Mohr's circle, while p gives the position of its center. s and p are the two invariants of the 2D Cauchy stress tensor

$$\boldsymbol{\sigma}_{2D} = \begin{bmatrix} \sigma_{xx} & \sigma_{xy} \\ \sigma_{xy} & \sigma_{yy} \end{bmatrix} \tag{10}$$

In plasticity, the yield limit surface is conveniently defined as the surface where the *yield function* $f(\boldsymbol{\sigma}_{2D})$ reaches 0 and is negative in the elastic domain. Here, the *yield function* is defined such as

$$f(\boldsymbol{\sigma}_{2D}) = s + p\sin\varphi - c\cos\varphi \tag{11}$$

Once the onset of plasticity is defined, one must describe the direction of the plastic flow rate. It is usual to define this rule through a plastic potential, $g(\boldsymbol{\sigma}_{2D})$, such that the plastic strain rate is directed along its gradient

$$\dot{\boldsymbol{\varepsilon}}^p_{2D} = \dot{\lambda}\frac{\partial g}{\partial \boldsymbol{\sigma}_{2D}} \tag{12}$$

where $\dot{\lambda}$ is called *plastic multiplier* and is always a non-negative parameter. Because of the underlying Coulomb friction, soil plasticity is generally "non-associated", meaning that f and g are independent. Given the way the Mohr-Coulomb yield function is written, following the same representation, the plastic potential is as follows

$$g(\boldsymbol{\sigma}_{2D}) = s + p\sin\psi \tag{13}$$

where ψ is the *dilatancy angle* of the material. This angle defines the ability of a granular media to dilate or contract when subjected to shear strain. For contraction, this angle is negative, while for expansion, it is positive. It can be rewritten as [32]

$$\psi = \arcsin\left(\frac{\dot{\varepsilon}^p_{vol}}{\dot{\varepsilon}^p_{dev}}\right) \tag{14}$$

where $\dot{\varepsilon}^p_{vol}$ is equal to the volumetric plastic strain rate (*i.e.*, $\dot{\varepsilon}^p_{vol} = \dot{\varepsilon}^p_{xx} + \dot{\varepsilon}^p_{yy}$), while $\dot{\varepsilon}^p_{dev}$ is the norm of the deviatoric plastic strain rate (*i.e.*, $\dot{\varepsilon}^p_{dev} = \sqrt{(\dot{\varepsilon}^p_{xx} - \dot{\varepsilon}^p_{yy})^2 + 4\dot{\varepsilon}^{p^2}_{xy}}$).

So far, the presentation was focused on the particular case of perfect plasticity where the plastic yield function and the plastic potential remain constant. However, in cases where such a limit varies, the evolution laws of the different parameters, defining *hardening* rules, are needed.

In granular media plasticity, the cohesion c and/or the friction angle φ, may vary along the plastic flow, leading to an "inflation" (or "deflation" in case of softening) of the elastic domain. In Mohr-Coulomb plasticity, compacity represents the most suitable internal variable that governs hardening during plastic deformation [33]. Hence the estimated mean cross section FVF ϕ_{2D}, defined as in equa-

tion (5), is exploited. The chosen hardening rules are given by

$$\varphi = \varphi(\phi_{2D}) \tag{15}$$

$$c = c(\phi_{2D}) \tag{16}$$

It is noteworthy that the cohesion c is related to the maximum tensile stress, denoted c', necessary to separate two particles (fibers here) from each other through

$$c = c' \cdot \tan\varphi \tag{17}$$

Based on this interpretation, it is proposed to keep c' constant throughout the compressive load. Thus, considering the hardening by the increase of the friction angle and, consequently, the cohesion c, it could be described only by equation (15).

The plastic consistency condition stipulates that, during plastic flow, the stress state, defined by a point in Mohr's plane, always remains on the yielding function limit ($f(\boldsymbol{\sigma}_{2D}) = 0$). As such, the differential of the yield function f must be set equal to zero

$$df = \frac{\partial f}{\partial \boldsymbol{\sigma}_{2D}} : \mathbb{C}^e_{2D} : (d\boldsymbol{\varepsilon}_{2D} - d\boldsymbol{\varepsilon}^p_{2D}) + \left(\frac{\partial f}{\partial \varphi} + \frac{\partial f}{\partial c}\frac{\partial c}{\partial \varphi}\right)\frac{\partial \varphi}{\partial \phi_{2D}}\frac{\partial \phi_{2D}}{\partial \varepsilon^p_{vol}} d\varepsilon^p_{vol} = 0 \tag{18}$$

with $\mathbb{C}^e_{2D}$ being the isotropic elastic stiffness tensor defined in 2D.

During the load step, at a given iteration $k+1$, a trial elastic state is initially calculated

$$\boldsymbol{\sigma}^{(k+1),tr}_{2D} = \boldsymbol{\sigma}^{(k)}_{2D} + \mathbb{C}^e_{2D} : d\boldsymbol{\varepsilon}_{2D} \tag{19}$$

If the plastic criterion is met (*i.e.*, the corresponding yield function $f^{tr} \geq 0$), one must estimate the induced plastic strain. By using the consistency condition, equation (18), and the plastic flow rule, equation (12), the plastic multiplier correction is obtained

$$\delta d\lambda \approx \frac{f^{tr}}{\frac{\partial f}{\partial \boldsymbol{\sigma}_{2D}} : \mathbb{C}^e_{2D} : \frac{\partial g}{\partial \boldsymbol{\sigma}_{2D}} - \left(\frac{\partial f}{\partial \varphi} + \frac{\partial f}{\partial c}\frac{\partial c}{\partial \varphi}\right)\frac{\partial \varphi}{\partial \phi_{2D}}\frac{\partial \phi_{2D}}{\partial \varepsilon^p_{vol}}\frac{\partial \varepsilon^p_{vol}}{\partial \lambda}} \tag{20}$$

which updates the plastic multiplier as

$$d\lambda^{(k+1)} = d\lambda^{(k)} + \delta d\lambda \tag{21}$$

Now, since the trial stress overpassed the yield surface, an update of the stress is necessary as well

$$\boldsymbol{\sigma}_{2D}^{(k+1)} = \boldsymbol{\sigma}_{2D}^{(k+1),tr} - \mathbb{C}_{2D}^{e} : \left(d\lambda \frac{\partial g}{\partial \boldsymbol{\sigma}_{2D}} \right) \tag{22}$$

and the elastoplastic consistent matrix necessary for solving the mechanical equilibrium

$$\mathbb{C}_{2D}^{ep} = \mathbb{C}_{2D}^{e} - \frac{\left(\mathbb{C}_{2D}^{e} : \frac{\partial g}{\partial \boldsymbol{\sigma}_{2D}} \right) \otimes \left(\mathbb{C}_{2D}^{e} : \frac{\partial f}{\partial \boldsymbol{\sigma}_{2D}} \right)}{\frac{\partial f}{\partial \boldsymbol{\sigma}_{2D}} : \mathbb{C}_{2D}^{e} : \frac{\partial g}{\partial \boldsymbol{\sigma}_{2D}} - \left(\frac{\partial f}{\partial \varphi} + \frac{\partial f}{\partial c} \frac{\partial c}{\partial \varphi} \right) \frac{\partial \varphi}{\partial \phi_{2D}} \frac{\partial \phi_{2D}}{\partial \varepsilon_{vol}^{p}} \frac{\partial \varepsilon_{vol}^{p}}{\partial \lambda}} \tag{23}$$

4.3. Identification procedure

As for the elastic part, the transversal Young modulus E_T identification is carried out by the computation of the slope of the unloading lines and is estimated as 20 MPa.

4.3.1. Dilatancy and friction angles

The FVF has been chosen as the internal variable when analyzing the plastic parameters. As plasticity is mobilized immediately, the plastic strains are approximately equivalent to the total ones. Hence, one can provide the horizontal strain ε_{xx}^{p} and vertical strain ε_{yy}^{p} from the experimental curves. Using the definition of the dilatancy angle ψ from equation (14) and assuming the measured strains as principal, the dilatancy angle reads

$$\psi = \arcsin\left(\frac{\dot{\varepsilon}_{vol}^{p}}{\dot{\varepsilon}_{dev}^{p}} \right) = \arcsin\left(\frac{d\varepsilon_{xx}^{p} + d\varepsilon_{yy}^{p}}{|d\varepsilon_{xx}^{p} - d\varepsilon_{yy}^{p}|} \right) = \arcsin\left(\frac{1 + \frac{d\varepsilon_{yy}^{p}}{d\varepsilon_{xx}^{p}}}{\left| 1 - \frac{d\varepsilon_{yy}^{p}}{d\varepsilon_{xx}^{p}} \right|} \right) \tag{24}$$

The result is shown in figure 10 for one example (T1100, dry). Let us note that the data corresponding to the lowest values of ϕ_{2D} come from very low levels of compression for which the estimate of the yarn width is the least reliable. The most important feature to be retained from this graph is the linear trend shown in red, where the critical state is reached at a value $\phi_{2D,cv}$

$$\psi(\phi_{2D}) = H(\phi_{2D} - \phi_{2D,cv}) \tag{25}$$

The evolution law of the friction angle is proposed to obey the Taylor's assumption [34], namely

$$\varphi = \psi + \varphi_{cv} \tag{26}$$

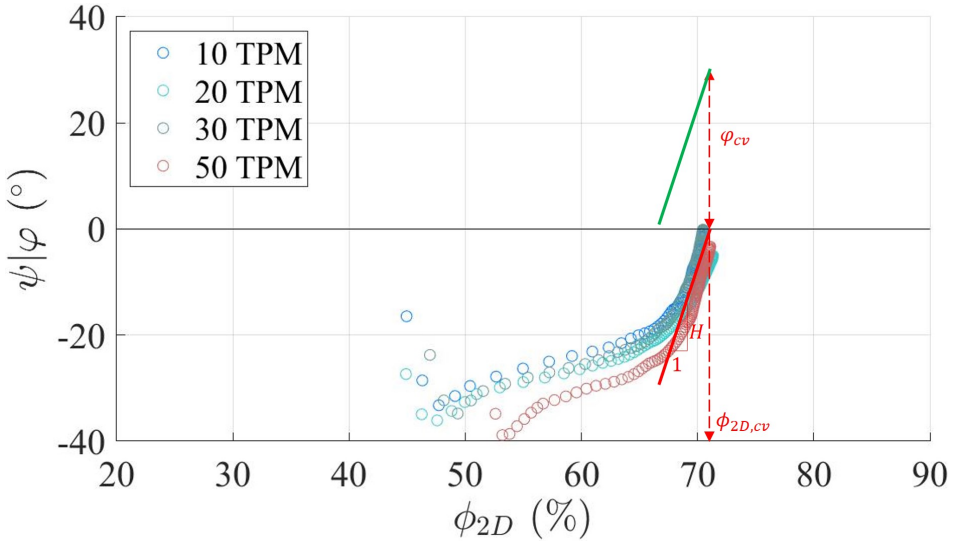

Figure 10: Evolution of the dilatancy and friction angles for the carbon yarn (ex. T1100, dry): the red line represents the simplification of the law to a straight line, while the green line is a consequence of Taylor's assumption.

where ψ is the dilatancy angle, and φ_{cv} is the friction angle at the critical state. The identified value is in agreement with the high values estimated experimentally on IM7 tows, by sliding a couple of tows parallel to each other ($\tan\varphi_{cv} \approx 0.6$) [35].

4.3.2. Cohesion

The identification of the cohesion law is more complex. It was earlier argued that c' could be read as a material property of the sizing (linked to the work necessary to separate two fibers). Hence, one can impose the yield criterion at the critical state, estimate c', and by knowing the value of φ, retrieve the evolution of the cohesion c (refer to the geometry of the Mohr-Coulomb locus in figure 9). Since the lateral borders of the yarn are free, the horizontal stress on average is $\sigma_{xx} = 0$. Therefore the traction limit is estimated as:

$$c' = \frac{\sigma_{yy}(1+\sin\varphi_{cv})}{2\sin\varphi_{cv}} \tag{27}$$

and the evolution of cohesion is calculated using equation (17). By computing a series of simulations and updating the vertical stress σ_{yy}, this value is progressively refined.

Let us emphasize that this discussion neglects the possible effect of the yarn twist which opposes a possible decohesion. As will be seen in the following discussion, twist does induce a notable increase in c', in an even more pronounced way than sizing.

4.3.3. Overview of identified values

Table 2 provides, for both yarn types, both in dry and wet conditions and for different twist levels, all the identified plastic parameters in the critical state.

The results show that the twist level does not much influence the final fiber volume fraction $\phi_{2D,cv}$ that the yarn can reach. Indeed, this "critical" state is expected to be very robust (unless the fiber diameters would be polydisperse). Besides, it can be observed that this critical state does not depend on whether the yarn is dry or wet.

Nevertheless, it is noticeable that the friction angle at this critical state φ_{cv} is greatly reduced (by 50%) by the lubricating effect of water. Again, no influence of the twist level or fiber type is observed on this parameter. In other words, the fiber arrangement (in the range of studied twist level) and type (mainly the sizing) do not impact the friction angle.

The identified hardening laws for each yarn type and water content conditions are seen to be described by a parameter assuming a constant value.

On the other hand, as expected, the cohesion parameter c' increases significantly according to the twist level with also significant variations between both dry and wet conditions. Indeed, c' is multiplied by about a factor 11 between 10 tpm to 50 tpm in dry condition and almost a factor 10 in wet conditions. Concerning the environmental conditions, for the IM7 fibers, c' is multiplied by at least a factor of 2 in wet conditions compared to the dry ones. This influence is less pronounced for T1100 fibers. However, in dry conditions for both fiber types, for a given twist level, c' remains invariant because the difference between sizing agents seems to be modest as compared to the fiber arrangement. Nevertheless, it is noticeable that, at a given twist level, the measurements show significant differences in wet conditions between both fiber types (up to +89% for IM7 twisted at 30 tpm). Let us stress that the IM7 fiber contains DGBA and pluronic F68 surfactant as sizing agents, whereas T1100 fiber contains only DGBA. Thus, although the influence of the sizing on c' is weaker than that of the twist level, when fixing the latter the influence of the water on the sizing could be highlighted. So, these subtle cohesion variations could help to clarify the influence of each parameter on the global mechanical behavior of the yarn. However, at this stage, it is too early to be definitive and these questions warrant further investigations under various conditions (*e.g.*, number of fibers per tow, different twists or additional lubricants).

4.4. Characterization of twist

The proposed constitutive law provides a complete description of the behavior of a parallel fiber bundle but does not include the effect of twist. Because the latter is usually a small perturbation, this

Fiber type	**IM7** ($\varnothing = 5.2$ µm)								**T1100** ($\varnothing = 5.5$ µm)							
Humidity	dry				wet				dry				wet			
tpm	10	20	30	50	10	20	30	50	10	20	30	50	10	20	30	50
$\phi_{2D,cv}$ (%)	71	71	71	71	71	71	71	71	71	71	71	71	71	71	71	71
φ_{cv} (°)	30	30	30	30	15	15	15	15	30	30	30	30	15	15	15	15
H (°/%)	6.7	6.7	6.7	6.7	10.0	10.0	10.0	10.0	6.7	6.7	6.7	6.7	10.0	10.0	10.0	10.0
c' (MPa)	0.3	0.6	0.85	3.4	0.7	1.2	1.8	6.9	0.3	0.6	0.85	3.4	0.55	0.7	0.95	5.6

Table 2: Identified parameters for two yarn types in different configurations.

Mohr-Coulomb description can be considered a first-order model.

In the experiments shown so far, the yarn is subjected to a tension of about $F = 6$ N — a value yarns typically are subjected to during weaving. This longitudinal force is assumed to be equally distributed among the $N = 48000$ fibers. To obtain orders of magnitude, the yarn is oversimplified as a cylinder of radius R, in which fibers have concentric helix geometries with the same pitch κ. Each fiber is assumed to be subjected to an equal tension force $f_z = F/N$. As due to the helical geometry, each fiber exerts a radial force directed toward the yarn axis, characterized by a distribution of body forces $\boldsymbol{b}$ as

$$\boldsymbol{b} = \frac{f_z}{R_c}\boldsymbol{n} \tag{28}$$

where R_c is the radius of curvature. As such, their radius of curvature $R_c(r)$, for a helix of radius r is

$$R_c(r) \approx \left(\frac{\kappa^2}{4\pi^2 r}\right) \approx 90 \text{ mm} \tag{29}$$

where κ represents the helix pitch (because $\kappa^2 \gg 4\pi^2 r^2$). Thus for the extreme helix, at 20 tpm, $\kappa = 50$ mm.

Exploiting a simple balance, the pressure inside the yarn shows a parabolic profile with a maximum in its center, $P = 4\pi^2 F/\kappa^2$, or about $P \approx 0.1$ MPa which is much lower than the stress induced by transversal compaction (of the order of 5 MPa). It is noteworthy that this pressure only depends on the axial force and the pitch. For the largest twist $\kappa = 20$ mm and still $F = 6$ N, the core pressure would be $P = 0.6$ MPa, just a factor 10 below the applied compression stress.

Hence, it can be concluded that the twist level becomes negligible within the compression range encountered by the yarn. Nevertheless, it is important to mention its importance for the yarn integrity as, in the absence of external constraints, twist plays a crucial role in preserving the structural strength and cohesion of the yarns.

5. Numerical results

This section presents the simulation of the experiments conducted on a T1100-type yarn under dry conditions, considering three levels of twist: 10, 30, and 50 tpm. Due to the challenging interpretation of low compression stages (highlighting a strong dependence on the preparation of the initial state), the analysis was focused on the largest compression forces (representative of the weaving and forming stages).

Indeed, the initial geometry of the yarn before compression is a difficulty (not only experimentally as discussed above, but also numerically). Starting from a circular geometry involves an initial computation where the contact area is to be determined at each load level, which is difficult in general and especially challenging for an elasto-plastic problem. However, the initial stage is soon forgotten. Thus, it is not useful to spend time resolving a very fragile problem, whereas only the robust results for high compression matter. Therefore, it has been decided to opt for an arbitrary choice where the contact area is already large to initiate our simulation. A further compression essentially erases the memory of this initial state. So, for all three twist levels, motivated by the large contact area of the yarn with both sapphire and metal plates, the cross section shape of the yarn is modeled as a race-track to avoid angular points.

Simulations were carried out on the final 0.3 mm of displacement d_y. Indeed, the dimensions of the section, along with the assumed homogeneity of the FVF throughout the section, were determined from the observed yarn profile at 0.3 mm. The lower plate was fixed, whereas the vertical displacement d_y of the upper plate was controlled to reach the desired loading. The friction coefficient between the yarn and the plates was assigned to $\mu = 0.1$. The yarn mean density is set at 1 g/cm^3. Let us emphasize that the twist is only accounted for through an effective cohesion c' as earlier discussed. The previously described elasto-plastic law was incorporated using the Abaqus/Explicit VUMAT subroutine.

Figure 11 shows the FVF values in the cross section of the simulated yarn in four principal frames. Although the FVF value is initially assumed homogeneous, it can be observed that a slightly larger density occurs in the lateral areas where shearing has been the most intense, approaching the critical state in these areas.

As noted in figure 12a, the experimental and numerical force-thickness curves are similar for all three twist levels in the loading and elastic unloading phases. Let us emphasize that, since this is an elasto-plastic model, a first phase of elastic compression is necessarily simulated in order to approach the experimental curve.

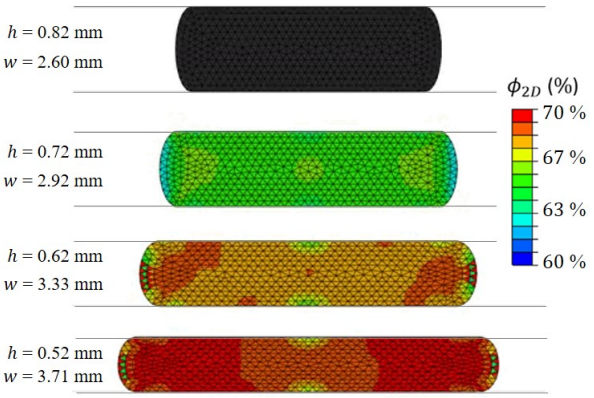

(a)

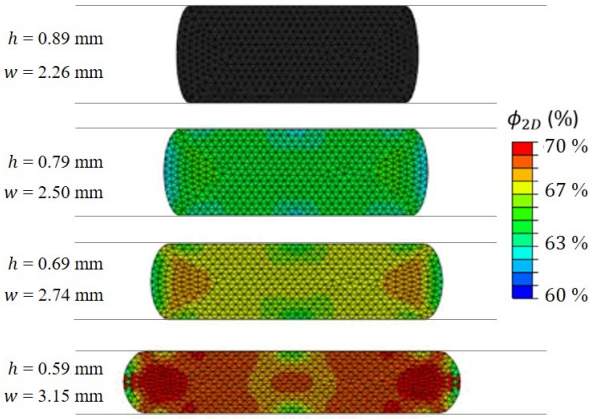

(b)

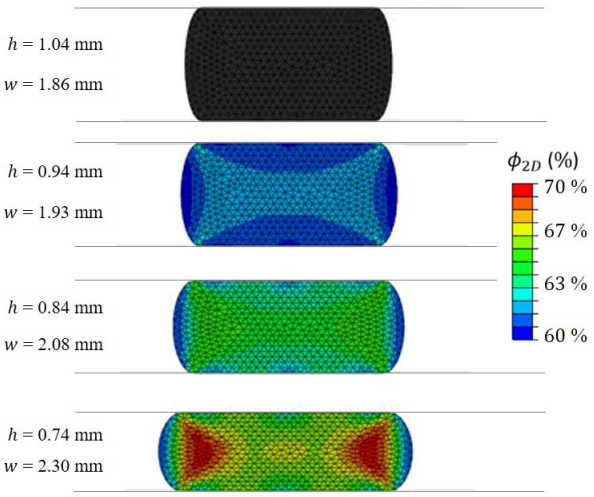

(c)

Figure 11: Simulation results on the T1100 yarn cross section FVF in the dry condition for: (a) 10, (b) 30 and (c) 50 tpm.

The growth of the average FVF with respect to the applied vertical stress also shows striking similarities with the experimental results (see figure 12b). However, the curves from the simulation, containing no difference in hardening law between the various twist levels, are closer to each other and reach the identified critical FVF with an almost identical curve. Using a linear hardening law for the friction and dilatancy angles has greatly smoothed out the curve as compared to the experimental one. Finally, it can be seen that the low compression levels do not coincide since the initial part of the compression was not simulated.

As the longitudinal and transverse directions can be considered essentially decoupled, the 2D Mohr-Coulomb plasticity model used to describe the transverse behavior of the yarn can be easily extended to a 3D complete simulation along with fiber longitudinal direction. Indeed, as discussed in the paper, carbon fibers can be considered as almost inextensible. Thus, the twisted yarn is then also itself mostly inextensible and only slight rearrangements of fibers may induce a small axial strain. Besides, the very small twist angle and the difficulty to mobilize inter-fiber slippage over long distances again favor a very high longitudinally stiffness.

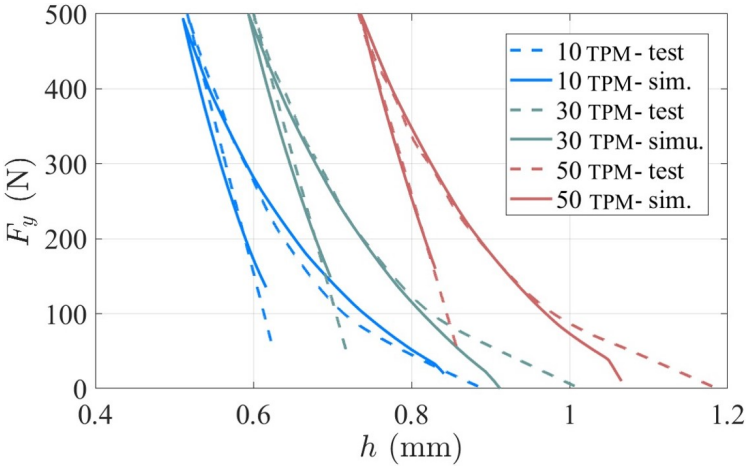

(a)

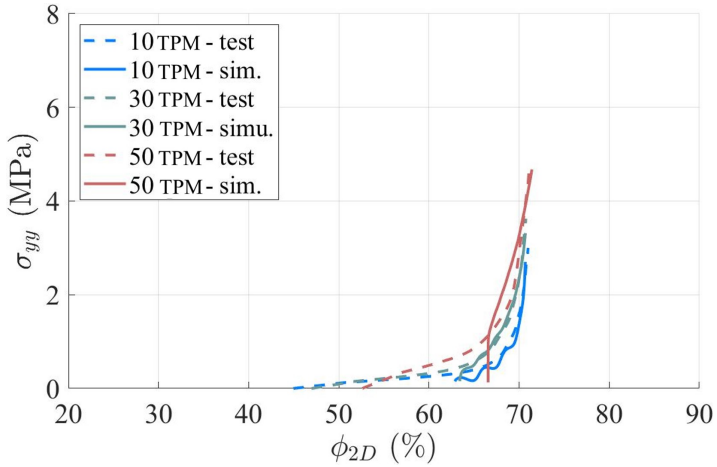

(b)

Figure 12: Comparison between the experimental and numerical results: (a) force-thickness curves (the same as the compaction machine response) and (b) the compaction curves and the evolution of the FVF confirming the null impact of twist onto the final fiber content in the critical state.

6. Conclusion

The diametral compression of yarns is a critical mechanical aspect of woven textiles that has been extensively studied in the literature. In this study, a compression test campaign to analyze the lateral profile of the yarn throughout the test has been conducted. The resulting curves revealed an elasto-plastic behavior and the occurrence of irreversible deformations within the cross section. Using a profilometer, the lateral profile images have provided information on thickness, width, and FVF (Fiber Volume Fraction).

However, due to experimental limitations (notably, the ability to observe only one side of the yarn profile), FVF measurement has been simplified by directly processing the width and thickness data. Additionally, the influence of twist level on yarn mechanical behavior has been investigated. Higher twist levels hindered the compression process and resulted in a more limited flattening of the yarn. Nevertheless, the observed FVF values remained relatively constant, indicating that the twist level did not significantly affect yarn compacity. This finding is crucial for optimizing yarn selection in weaving applications.

Furthermore, the presence of water had a significant impact on the mechanical behavior of the yarn. Compared to dry yarn, the introduction of water decreased the critical friction angle. Water acted as a lubricant, facilitating the mutual sliding of fibers during compression.

Overall, the experimental observations led to a homogenized behavior law that differs from widespread hyper- or hypo-elastic models. The Mohr-Coulomb elasto-plastic law in the section plane, akin to that observed in 2D granular media, offers not only a natural frame of description for these irreversible changes but also involves a drastic reduction in the number of constitutive parameters needed.

Additionally, the experimental results (together with Taylor's assumption) have led to a hardening law for cohesion based on the evolution of the friction angle and dilatancy during compression. Simulation results of yarn cross sections with different twist levels validated the experimental results, as evidenced by force-thickness and FVF compaction curves.

In the current model, yarn twist only appears heuristically through an effective cohesion. Ideally, a more accurate description of each fiber path should couple longitudinal tension and cohesion from a distribution of body forces in each cross section.

Acknowledgments

Marcello Rubino acknowledges the support of a PhD grant N°2019/1662 from ANRT and Safran Aircraft Engines.

References

[1] G. Marsh, Aero engines lose weight thanks to composites, Reinforced Plastics 56 (2012) 32–35.

[2] M. Patel, B. Pardhi, S. Chopara, M. Pal, Lightweight Composite Materials for Automotive - A Review, Concepts Journal of Applied Research 3 (2018) 1–9.

[3] I. Gnaba, X. Legrand, P. Wang, D. Soulat, Through-the-thickness reinforcement for composite structures: A review, Journal of Industrial Textiles 49 (2019) 71–96.

[4] A. Mouritz, M. Bannister, P. Falzon, K. Leong, Review of applications for advanced three-dimensional fibre textile composites, Composites Part A: Applied Science and Manufacturing 30 (1999) 1445–1461.

[5] A. Mouritz, B. Cox, A mechanistic interpretation of the comparative in-plane mechanical properties of 3d woven, stitched and pinned composites, Composites Part A: Applied Science and Manufacturing 41 (2010) 709–728.

[6] M. N. Saleh, C. Soutis, Recent advancements in mechanical characterisation of 3d woven composites, Mechanics of Advanced Materials and Modern Processes 3 (2017) 1–17.

[7] P. Bussetta, N. Correia, Numerical forming of continuous fibre reinforced composite material: A review, Composites Part A: Applied Science and Manufacturing 113 (2018) 12–31.

[8] B. Liang, P. Boisse, A review of numerical analyses and experimental characterization methods for forming of textile reinforcements, Chinese Journal of Aeronautics 34 (2021) 143–63.

[9] J. Xie, Z. Guo, M. Shao, W. Zhu, W. Jiao, Z. Yang, L. Chen, Mechanics of textiles used as composite preforms: A review, Composite Structures 304 (2023) 116401.

[10] P. Boisse, Y. Aimene, A. Dogui, S. Dridi, S. Gatouillat, N. Hamila, M. A. Khan, T. Mabrouki, F. Morestin, E. Vidal-Sallé, Hypoelastic, hyperelastic, discrete and semi-discrete approaches for textile composite reinforcement forming, International Journal of Material Forming 54 (2010) 1229–1240.

[11] S. Mathieu, P. Boisse, N. Hamila, F. Bouillon, Locking and Stability of 3D Woven Composite Reinforcements, Key Engineering Materials 611-612 (2014) 292–299.

[12] S. Mathieu, N. Hamila, F. Dupé, C. Descamps, P. Boisse, Stability of 3D Textile Composite Reinforcement Simulations: Solutions to Spurious Transverse Modes, Applied Composite Materials 23 (2016) 739–760.

[13] B. Chen, J. Colmars, N. Naouar, P. Boisse, A hypoelastic stress resultant shell approach for simulations of textile composite reinforcement forming, Composites Part A: Applied Science and Manufacturing 149 (2021) 106558.

[14] J. Li, N. Hamila, E. Guzman-Maldonado, G. L'Hostis, P. Wang, Improved hyperelastic model for simulating the forming of biaxial braided fabrics, 2023.

[15] B. Chen, J. Colmars, R. Bai, N. Naouar, P. Boisse, Kinematic modeling of transverse shear in textile composite reinforcements forming, International Journal of Mechanical Sciences 245 (2023) 108129.

[16] M. Li, K. Liu, J. Ge, J. Xie, Z. Liu, B. Zhang, J. Huang, J. Liang, A novel modeling method for the mechanical behavior of 3D woven fabrics considering yarn distortion, Composites Science and Technology 230 (2022) 109691.

[17] Z. Gao, L. Chen, A review of multi-scale numerical modeling of three-dimensional woven fabric, Composite Structures 263 (2021) 113685.

[18] Y. Wielhorski, A. Mendoza, M. Rubino, S. Roux, Numerical modeling of 3D woven composite reinforcements: A review, Composites Part A: Applied Science and Manufacturing 154 (2022) 106729.

[19] A. Charmetant, E. Vidal-Sallé, P. Boisse, Hyperelastic modelling for mesoscopic analyses of composite reinforcements, Composites Science and Technology 71 (2011) 1623–1631.

[20] E. De Luycker, N. Hamila, Modeling of hyperelastic bending of fibrous media using second-gradient isogeometric analysis: Weaving and braiding applications, Composites Part A: Applied Science and Manufacturing 167 (2023) 107415.

[21] P. Badel, E. Vidal-Sallé, E. Maire, P. Boisse, Simulation and tomography analysis of textile composite reinforcement deformation at the mesoscopic scale, Composites Science and Technology 68 (2008) 2433–2440.

[22] G. Zhou, X. Sun, Y. Wang, Multi-chain digital element analysis in textile mechanics, Composites Science and Technology 64 (2004) 239–244.

[23] D. Durville, Simulation of the mechanical behaviour of woven fabrics at the scale of fibers, International Journal of Material Forming 3 (2010) 1241–1251.

[24] S. D. Green, A. C. Long, B. S. El Said, S. R. Hallett, Numerical modelling of 3D woven preform deformations, Composite Structures 108 (2014) 747–756.

[25] D. Durville, I. Baydoun, H. Moustacas, G. Périé, Y. Wielhorski, Determining the initial configuration and characterizing the mechanical properties of 3D angle-interlock fabrics using finite element simulation, International Journal of Solids and Structures 154 (2018) 97–103.

[26] Z. Yang, Y. Jiao, J. Xie, L. Chen, W. Jiao, X. Li, M. Zhu, Modeling of 3D woven fibre structures by numerical simulation of the weaving process, Composites Science and Technology 206 (2021) 108679.

[27] H. Xiao, O. T. Bruhns, A. Meyers, Hypo-Elasticity Model Based upon the Logarithmic Stress Rate, Journal of Elasticity 47 (1997) 51–68.

[28] M. Schneebeli, Mechanique des soils-une analogie mechanique pour les terres sans cohesion, Comptes Rendes Hebdomaires des Seances de l'Academie des Sciences 243 (1956) 125–126.

[29] J. J. Moreau, P. D. Panagiotopoulos, Nonsmooth mechanics and applications, volume 302, Springer, 2014.

[30] B. Cambou, M. Jean, F. Radjaï, Micromechanics of granular materials, John Wiley & Sons, 2013.

[31] E. A. de Souza Neto, D. Peric, D. R. J. Owen, Computational Methods for Plasticity: Theory and Applications, Wiley, 2008.

[32] K. H. Roscoe, The Influence of Strains in Soil Mechanics, Géothecnique 20 (1970) 129–170.

[33] S. Roux, F. Radjai, Texture-dependent rigid-plastic behavior, Physics of Dry Granular Media (1998) 229–236.

[34] P. W. Rowe, The stress-dilatancy relation for static equilibrium of an assembly of particles in contact, Proc. R. Soc. Lond. 269 (1962) 500—-527.

[35] M. Tourlonias, M.-A. Bueno, G. Fassi, I. Aktas, Y. Wielhorski, Influence of friction angle between carbon single fibres and tows: Experimental analysis and analytical model, Composites Part A: Applied Science and Manufacturing 124 (2019) 105478.